Flow and rheology of suspensions of two-dimensional cylindrical or anisotropic particles with Navier slip

Kamal, Catherine; Botto, Lorenzo

DOI
10.1103/PhysRevFluids.9.074102

Publication date
2024

Document Version
Final published version

Published in
Physical Review Fluids

Flow and rheology of suspensions of two-dimensional cylindrical or anisotropic particles with Navier slip

Catherine Kamal [1] and Lorenzo Botto[2]
[1]*Cambridge Graphene Centre, University of Cambridge, Cambridge CB3 0FA, United Kingdom*
[2]*Process and Energy Department, Faculty of Mechanical Engineering, TU Delft, 2628 CD Delft, The Netherlands*

(Received 3 October 2023; accepted 10 June 2024; published 15 July 2024)

Through boundary integral simulations, we investigate, in the creeping flow limit and in the absence of Brownian noise, the effects of Navier slip on the orientational dynamics and effective shear viscosity of a semidilute suspension of two-dimensional particles with either circular or elongated (platelike) shape, interacting only via hydrodynamic and contact forces. We have recently shown that it is theoretically possible for a dilute system of slip platelike particles to display an effective shear viscosity smaller than the viscosity of the suspending fluid. This large viscosity reduction is primarily due to the suppression of the tumbling motion predicted for a no-slip particle and the attainment of a stable orientation. In this paper, we show that the effect of particle-particle interaction at semidilute concentrations is to cause the particles to fluctuate about the stable orientation and, above a threshold solid fraction c_{crt}, to tumble. As a consequence, a sharp increase in the effective shear viscosity with solid fraction c occurs for $c > c_{\mathrm{crt}}$. Our results suggest that, for a given particle aspect ratio, there is a value of c that maximizes the reduction in the effective shear viscosity of the suspension.

DOI: 10.1103/PhysRevFluids.9.074102

I. INTRODUCTION

Recent experiments on semidilute suspensions of graphene oxide nanoparticles show a nonmonotonic dependence of the effective shear viscosity on solid fraction in a range of high shear rates [1,2]. This result is not expected from classical suspension theory, which predicts a monotonic increase with particle solid fraction [3]. A nonmonotonic change of viscosity on solid fraction was also reported for platelike particles in Refs. [4,5]. Two-dimensional nanomaterials, such as graphene oxide, are platelike particles of atomic thickness. Therefore, accounting for the anisotropic particle shape could be essential for explaining the observed dependence.

We have recently shown, through both continuum and molecular dynamics simulations of single platelike particles in shear flow, that in the dilute limit, a possible explanation for a decreasing shear viscosity for increasing solid fraction is a violation of the no-slip boundary condition [6–9]. Nanomaterials, such are graphene, are plate-like nanoparticles that can present significant hydrodynamic slip at their surface when in contact with water and other solvents [10–12], with slip lengths often larger than the nanoparticle thickness. For this range of slip lengths, the hydrodynamic slip changes the stress distribution on the planar surface of the particles, leading to a suppression of the classical tumbling motion predicted by Jeffery's theory for no-slip particles [13]. Specifically, based on theory

and simulations, we predicted that at high rotational Péclet numbers (Pe), a single particle featuring a slip length larger than the particle thickness aligns indefinitely at a relatively small, constant angle with respect to the flow direction [6–9,14]. This change in orientational microstructure can directly impact the effective shear viscosity of the suspension [15].

The current paper analyzes numerically, in the infinite Péclet number regime, the effect of hydrodynamic interactions on the orientational microstructure and effective shear viscosity of a suspension of particles with Navier slip surfaces. The particles are assumed to be two-dimensional and to move in the flow-gradient plane. The basic question we would like to address is how the effect of hydrodynamic interactions at finite volume fractions changes the dilute-limit prediction of a stable orientation and how this in turn affects the effective viscosity. Because the code can recover the case of cylinders for an aspect ratio equal to one, we also analyzed the shear viscosity of a suspension of two-dimensional cylinders with slip, a problem which both furnishes a validation case for the numerical code and offers interesting fluid dynamic insights. We address the numerical challenge of simulating suspensions of large aspect ratio particles by using a two-dimensional boundary integral method for incompressible Stokes flow [16]. The high accuracy of the boundary integral method in resolving the stress over the particle surface [16,17] allows us to consider suspensions with particles of relatively small thickness and resolve near contact interactions.

At dilute concentration, hydrodynamic slip has been found to reduce the effective viscosity η^{eff} compared to an identical suspension of no-slip particles. The magnitude of this reduction depends on Pe, the particle aspect ratio, and the ratio of slip length λ to the particle thickness [7,15,18–20]. Allision [18] computed η^{eff} for noninteracting ellipsoidal particles using the continuum boundary integral formulation [16] and found that, for small Pe, η^{eff} is significantly smaller for perfect-slip ellipsoids ($\lambda \to \infty$) than for no-slip ellipsoids ($\lambda = 0$). For noninteracting spheres, Luo and Pozrikidis [20] showed analytically that increasing λ reduces η^{eff} for all values of Pe; for a fluid of viscosity η and particle solid fraction $c \ll 1$, η^{eff} decreases from $\eta^{\text{eff}}/\eta = 1 + (2/5)c$ in the no-slip case to $\eta^{\text{eff}}/\eta = 1 + c$ in the perfect-slip case [20]. Using a continuum boundary integral formulation for incompressible Stokes flow, we have recently shown for a dilute suspension of slender noninteracting two-dimensional particles that hydrodynamic slip could cause η^{eff} to be smaller than η [15]. This regime occurs provided that λ is larger than the half-thickness of the particle and Pe is sufficiently large. A physical explanation for this unusual viscosity reduction is the stable alignment: for a particle oriented almost in the flow direction and not rotating, the Navier slip velocity reduces the viscous friction between parallel fluid layers provided that the particle is sufficiently thin so as not to significantly disturb the flow streamlines. The suppression of rotation is key. If each particle in the suspension was continuously rotating, such a large viscosity reduction would not be observed despite the slip-induced reduction in frictional viscous forces on the particle surface.

At semidilute concentrations, particle-particle interactions become important (a discussion of the semidilute regime for anisotropic particles is given in Refs. [21,22]). Numerical simulations of no-slip platelike particles [23–27] and experiments with no-slip oblate ellipsoids [28] demonstrate an increase in particle alignment with the flow direction as the solid fraction increases, and the concurrent formation of particle clusters. Because of the added hydrodynamic stress induced by particle-particle interaction, the effective shear viscosity for no-slip particles increases with the solid fraction more than linearly.

Studies on slip particles in the semidilute limit are more rare. The effect of hydrodynamic slip at semidilute concentration has been studied in Ref. [7] through molecular dynamics simulations of disklike aromatic molecules (hexabenzocoronene) of length-to-thickness aspect ratio $a/b = 3$, slip length larger than b, and for an extensive range of Pe. The particles are suspended in water. The simulations showed that hydrodynamic slip dramatically reduced η^{eff} for an extensive range of Pe. At large Pe, the rate of change of η^{eff} with the solid fraction was smaller for a slip molecule than that for a no-slip molecule having the same geometry, an effect which could be probed by changing the solid-liquid molecular interaction potential in the molecular dynamic simulation. By investigating the pairwise interaction of two spherical particles, Luo and Pozrikidis [19] showed by

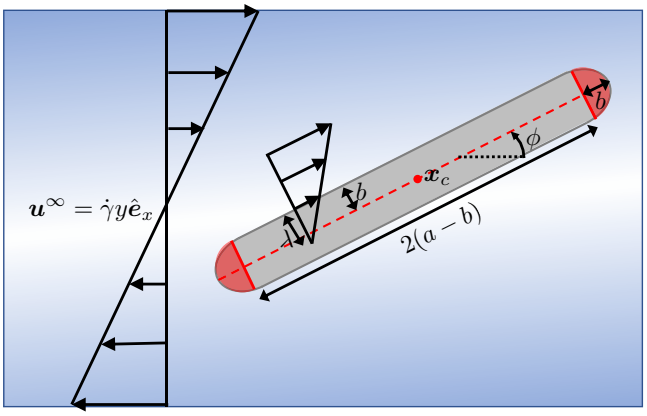

FIG. 1. Sketch of a two-dimensional slender Navier slip particle suspended in an external shear flow field.

continuum simulations that at semidilute concentrations the presence of a finite Navier slip velocity leads to a significant reduction in the rate of increase of η^{eff} with solid fraction c. The increase in η^{eff} with c was an order of magnitude smaller for the slip spheres than for no-slip spheres. For these two cases, hydrodynamic slip thus reduces the effect of particle-particle interaction on η^{eff} at higher solid fractions. Whether this trend applies to platelike particles remains an open question that this paper aims to address.

The outline of this paper is as follows. In Sec. II we present the mathematical model for computing the particle dynamics and suspension rheology by solving dynamically the boundary integral equation of Stokes flow. The numerical implementation of this model is then given in Sec. III. In Sec. IV an analytical solution for η^{eff} for particles with $a/b = 1$ is developed and compared with our numerical model (analytical solutions for the effective viscosity of no-slip cylinders at dilute and semidilute concentration are available in the literature [29,30]). This section contains new results for cylinders and is used for validation before tackling the more complex shape of a slender platelike particle. Finally, in Sec. V we use our numerical model to study the dynamics and rheological behavior of slender particles with nonzero Navier slip lengths at semidilute concentrations.

II. THEORETICAL PRELIMINARIES ON THE DYNAMICS AND EFFECTIVE SHEAR VISCOSITY OF TWO-DIMENSIONAL PARTICLES

We consider a sheared suspension of N identical rigid particles. The particles are suspended in an external shear flow field, given in a Cartesian coordinate system as $\boldsymbol{u}^\infty = \dot{\gamma} y \hat{\boldsymbol{e}}_x$, where $\hat{\boldsymbol{e}}_x$ is the unit vector in the flow direction, y points in the direction of the unit vector $\hat{\boldsymbol{e}}_y$ perpendicular to the flow, and $\dot{\gamma}$ is the shear rate. The velocity field $\boldsymbol{u}$, the pressure field p, and the corresponding stress tensor field $\boldsymbol{\sigma}^b$ are assumed to satisfy the incompressible Stokes equations:

$$\nabla \cdot \boldsymbol{\sigma}^b = 0, \quad \sigma^b_{ij} = -\delta_{ij} p + \eta \left(\frac{\partial u_i}{\partial x_j} + \frac{\partial u_j}{\partial x_i} \right), \quad \nabla \cdot \boldsymbol{u} = 0, \tag{1}$$

where η is the viscosity of the fluid.

Each particle is modeled as a two-dimensional object (in the $\hat{\boldsymbol{e}}_x$, $\hat{\boldsymbol{e}}_y$ plane) consisting of a rectangle of half-length $a - b$ and half-thickness b, with semicircular ends of radius b, as illustrated in Fig. 1. This shape is motivated by the analysis of the surface that best approximates a graphene nanoparticle's cross-sectional surface from a hydrodynamic viewpoint, as suggested by molecular dynamics simulations of single-layer graphene in water [6,8]. This parametrization also enables one to simulate particles with a circular cross section simply by setting $a = b$. The length-to-thickness

aspect ratio of the particle is a/b. In the laboratory frame (fixed with respect to $\hat{\boldsymbol{e}}_x$ and $\hat{\boldsymbol{e}}_y$), the configuration of the kth particle is given by the position of the particle's central point $\boldsymbol{x}_c[k]$ and the particle's orientation angle $\phi[k]$. Here, $\phi[k]$ is defined as the anticlockwise angle from $\hat{\boldsymbol{e}}_x$ to the long axis of the particle.

On the surface $L[k]$ of the kth particle, the Navier slip boundary condition

$$\boldsymbol{u}^{\mathrm{sl}}[k] = \frac{\lambda}{\eta}\boldsymbol{n}[k] \times \boldsymbol{f}[k] \times \boldsymbol{n}[k] \tag{2}$$

is prescribed, where λ is the Navier slip length, $\boldsymbol{n}[k]$ is the unit normal vector pointing outwards from the surface of the particle, $\boldsymbol{u}^{\mathrm{sl}}[k]$ is the Navier slip velocity, and $\boldsymbol{f}[k] = \boldsymbol{\sigma}^b \cdot \boldsymbol{n}[k]$ is the surface traction. The particles are considered to be torque-and-force free, so each particle moves according to a rigid body motion $\boldsymbol{U}[k] + \Omega[k]\hat{\boldsymbol{e}}_z \times (\boldsymbol{x} - \boldsymbol{x}_c[k])$. Here, $\boldsymbol{U}[k]$ is the particle's translational velocity and $\Omega[k]$ is the particle's angular velocity.

Our primary interest is to compute the instantaneous effective viscosity of the suspension and its time average value $\langle \eta^{\mathrm{eff}} \rangle$, where $\langle \cdot \rangle$ indicates time averaging. The instantaneous effective viscosity can be calculated from [16,25,26,31]

$$\eta^{\mathrm{eff}}/\eta = 1 + \sigma_{xy}, \quad \sigma_{xy} = \frac{c}{\dot{\gamma}\eta A_p N}\sum_{k=1}^{N} S_{xy}[k]. \tag{3}$$

Here, A_p is the cross-sectional area of each particle, c is the solid fraction (defined in Sec. III), and S_{xy} is the off-diagonal component of the stresslet tensor, defined as

$$S_{xy}[k] = \frac{1}{2}\int_{L[k]} \left[f_x y + f_y x - 2\eta\left(u_x^{\mathrm{sl}} n_y + u_y^{\mathrm{sl}} n_x\right)\right] \mathrm{d}L, \tag{4}$$

where $\mathrm{d}L$ is an infinitesimal line element. The stresslet tensor is time dependent, since $\boldsymbol{f}[k]$ and $\boldsymbol{u}^{\mathrm{sl}}[k]$ depend on the instantaneous configuration of the particles. For conciseness, from here on we have dropped the particle index notation k in all integral expressions.

An isolated particle with $b \lessapprox \lambda$ aligns with the flow at a small constant orientation angle ϕ_c [6,8]. For λ approximately smaller than b, the particle spends most of its rotation time aligned with the direction of flow before tumbling, creating a periodic orbit [13]. One way to distinguish a stable orientation from a rotational behavior is to measure the time-average mean and standard deviation of $\phi = \sum_{k=1}^{N} \phi[k]/N$. These are defined as

$$\bar{\phi} = \langle \phi \rangle, \quad \mathrm{SD}(\phi) = \langle (\phi - \bar{\phi})^2 \rangle, \tag{5}$$

respectively. A particle instantaneously aligned at $\phi = \phi_c$ is characterized by $\bar{\phi} = \phi_c$ and $\mathrm{SD}(\phi) = 0$, whereas a rotating particle has $\bar{\phi} = 0$ and a finite value of $\mathrm{SD}(\phi)$ [7,8]. The longer the rotational time period of the particle, the smaller $\mathrm{SD}(\phi)$.

Another quantity of interest is the mean tangential force $\langle F_s \rangle$ acting on the top-half surface $L^+[k]$ of each particle. This quantity is useful to predict the minimum shear rate for layered particles to break up under a hydrodynamic shear [32,33], as required in many 2D nanomaterial production methods such as microfluidization [34,35] and high shear mixing [36,37]. The calculation of $\langle F_s \rangle$ requires calculating the instantaneous shear (in the direction $\hat{\boldsymbol{e}}_s$) force acting on the top-half surface L^+ of the kth particle:

$$F_s[k] = \int_{L^+[k]} \boldsymbol{f} \cdot \hat{\boldsymbol{e}}_s \mathrm{d}L. \tag{6}$$

The top-half of the particle corresponds to the surface of the particle above the dashed line in Fig. 1. To define $L^+[k]$ explicitly, we first parametrize the surface $L[k]$ of each particle in its body-fixed frame of reference $(\hat{\boldsymbol{e}}_s, \hat{\boldsymbol{e}}_n)$ as $L[k] = (s[k], \pm h(s[k]))$, where $-a \leqslant s[k] \leqslant a$. Here $s[k]$ is the distance running along the long particle axis and passing through the center of the particle (the dashed line in Fig. 1), $h(s[k])$ is the thickness of the particle, and $\hat{\boldsymbol{e}}_s, \hat{\boldsymbol{e}}_n$ are orthogonal unit

vectors, with $\hat{\boldsymbol{e}}_s$ oriented in the direction of the particle's long axis. The top-half of the surface is thus $L^+[k] = (s[k], h(s[k]))$. The mean tangential force $\langle F_s \rangle$ corresponds to the time average of $F_s = \sum_{k=1}^{N} F_s[k]/N$.

III. NUMERICAL IMPLEMENTATION

We perform dynamic simulations of suspensions of N identical two-dimensional particles in a doubly periodic square computational domain of area A. The solid fraction of the suspension is defined as $c = NA_p/A$, where A_p is the area of each particle. The double periodicity of the domain is implemented using the Lees-Edwards periodic boundary condition [38]. This boundary condition is used to limit boundary effects on the microstructure that would be incurred with the use of solid external walls [39].

Calculating η^{eff}, $\bar{\phi}$, and F_s requires $\boldsymbol{f}[k]$, $U[k]$, and $\Omega[k]$, for $k = 1 : N$, as a function of time. We compute these quantities at a given time t by solving the boundary integral equations of incompressible Stokes flow supplemented with the Navier slip boundary condition, Eq. (2), applied on each particle's surface $L[k]$ [6,8]. For each point $\boldsymbol{x}_1 \in L[k]$, the boundary integral representation gives

$$\sum_{k=1}^{N}\left[\frac{1}{4\pi}\int_{L[k]} \boldsymbol{n}(\boldsymbol{x})\cdot\boldsymbol{K}(\boldsymbol{x}-\boldsymbol{x}_1)\cdot\boldsymbol{u}^{\text{sl}}(\boldsymbol{x})\mathrm{d}L(\boldsymbol{x}) - \frac{1}{4\pi\eta}\int_{L[k]}\boldsymbol{G}(\boldsymbol{x}-\boldsymbol{x}_1)\cdot\boldsymbol{f}(\boldsymbol{x})\mathrm{d}L(\boldsymbol{x})\right]$$
$$= U[k] + \Omega[k]\times(\boldsymbol{x}_1 - \boldsymbol{x}_c[k]) + \frac{\boldsymbol{u}^{\text{sl}}(\boldsymbol{x}_1)}{2} - \boldsymbol{u}^{\infty}(\boldsymbol{x}_1), \tag{7}$$

where $\mathbf{n}(\boldsymbol{x})$ is the unit surface normal at position $\boldsymbol{x}$ pointing into the fluid. The second-order tensor $\boldsymbol{G}$ and the third-order tensor $\boldsymbol{K}$ correspond to the two-dimensional, double-periodic Green's functions of incompressible Stokes flow [16,40]. Equation (7) represents a linear system of equations for the variables $\{\boldsymbol{f}[k], U[k], \Omega[k]\}$. To close this system, further conditions of zero force and torque acting on each particle are required:

$$\boldsymbol{F}[k] = \int_{L[k]} \boldsymbol{f}\,\mathrm{d}L = 0, \quad T[k] = \hat{\boldsymbol{e}}_z \cdot \int_{L[k]} (\boldsymbol{x}_1 - \boldsymbol{x}_c)\times\boldsymbol{f}\,\mathrm{d}L = 0. \tag{8}$$

To solve the coupled Eqs. (7) and (8), we follow the procedure outlined in Refs. [6,8]. In summary, the surface of each kth particle is divided into N_p subintervals. The functions $\boldsymbol{f}[k]$ and $\boldsymbol{u}^{\text{sl}}[k]$ are then discretized as piecewise constant functions with each variable centered at the midpoint of each subinterval. The discretization of Eqs. (7) and (8) results in a set of $N(2N_p + 3)$ linear equations for the variables $\mathbf{X} = \{\boldsymbol{f}[k]_1, \ldots, \boldsymbol{f}[k]_{N_p}, \boldsymbol{U}[k], \Omega[k]\}$ with $k = 1 : N$; here, $\boldsymbol{f}[k]_l$ is the discrete value of $\boldsymbol{f}$ on subinterval l of particle k. The set of linear equations is then solved by using Gaussian elimination. The numerical solution for $\boldsymbol{f}[k]$ is defined up to a normal force contribution $p_0\boldsymbol{n}[k]$. Here, p_0 is an arbitrary pressure. To find a unique solution, we set $p_0 = 0$ by using the preconditioning method described by Pozrikidis [40].

For a large number of particles, the size of the system quickly becomes very large. In this case, the linear matrix ($\boldsymbol{A}\cdot\mathbf{X} = \boldsymbol{b}$) can be solved by an iterative method. For the mth iteration, we use the scheme described by Pozrikidis [40]:

$$\boldsymbol{D}\cdot\mathbf{X}^{m+1} - (\boldsymbol{D} - \boldsymbol{A})\cdot\mathbf{X}^{m} = \boldsymbol{b}.$$

Here, $\boldsymbol{D}$ represents diagonal blocks containing particle clusters. A "cluster" is a set of particles separated by a minimum separation distance of at most $2\epsilon_d$, where ϵ_d is a separation factor.

Following Pozrikidis [25], we use $\epsilon_d = a/10$ (for a fixed a); for smaller values of ϵ_d the time-marching algorithm becomes very stiff, requiring very small time steps. Also, we use $N = 16$ unless otherwise stated. We use a nonuniform surface grid with more points on the curved edge regions than on the slender surface of each particle, as described in Ref. [8]. The number of grid points per element ranges from $N_p = 24$ for $a/b = 1$ to $N_p = 72$ for $a/b = 50$. These values of N_p were

chosen to ensure grid convergence, as measured by the calculation of η^{eff}, for a fixed array of the particles at $c = 0.3$ for $a/b = 1$, $c = 0.1$ for $a/b = 10$, and $\hat{c} = N\pi a^2/A = 0.1$ (The meaning of $\hat{c}$ will be explained in Sec. V B 3) for $a/b = 20$ and $a/b = 10$. Validation of our model for $a/b = 1$ is presented in Sec. IV, and convergence and validation studies for $a/b = 10$, 20, and 50 are presented in Sec. V.

The initial configuration of all the particles is produced by perturbing, according to computer-generated random numbers, the orientation and center location of a regular array of particles separated by an assigned distance $\boldsymbol{d}$. The distance $\boldsymbol{d}$ is selected so that the centers of the particles form a regular periodic array. The random number for the particle orientation angle ranges between 0 and π, and for the two coordinates of the particle center between $\pm d/2$.

The configuration of the N particles is advanced in time by an explicit second-order scheme (the Richardson time step; cf. [41]). To prevent overlap of the particles at any time step, a geometric exclusion method is implemented, as described by Pozrikidis [25]. In summary, this method involves first expanding the surface of each particle by an amount $1 + \epsilon_d$, and then testing for overlaps. The maximum time step is chosen to ensure that the overlap between the region bounded by the extended surfaces of the particles never exceeds ϵ_d . If an overlap is found between the expanded surfaces of the particles, including the periodic images, then the centers of each pair of overlapping particles are displaced by an amount ϵ_d along the vector of minimum separation. Such displacement is equivalent to imposing a repulsive force that keeps the particles separated by a surface-to-surface distance ϵ_d. If the overlap occurs in a cluster of two particles, the particles' centers are displaced symmetrically. Otherwise, the particles' centers are displaced antisymmetrically by fixing the first particle in the cluster and displacing the neighboring particles. This procedure is adopted to prevent an infinite loop of particles "bouncing" off each other [25].

To ensure that the time averages do not depend on the initial condition, statistical averages are calculated after a long time T. We set T equal to the time required for an isolated no-slip particle of the given aspect ratio to complete one entire tumbling cycle. This time is chosen based on a previous study by Pozrikidis on the time taken for an aligned state to become fully randomized [26].

IV. EFFECTIVE SHEAR VISCOSITY FOR TWO-DIMENSIONAL CYLINDERS WITH SLIP

For the case $a/b = 1$, which corresponds to cylinders of infinite extent in the vorticity direction, numerical values of $\langle\eta^{\text{eff}}\rangle$ in the semidilute limit can be compared directly to analytical estimates. A Taylor expansion of the effective viscosity for $c \ll 1$ gives

$$\langle\eta^{\text{eff}}\rangle/\eta = 1 + \alpha c + \beta c^2 + O(c^3). \tag{9}$$

The coefficient α, commonly referred to as the intrinsic viscosity, corresponds to the stress generated by an isolated, freely suspended particle. Its value has been calculated analytically for no-slip [29,42] and slip cylinders [15]. For a Navier slip boundary condition with slip length λ, α decreases with λ according to

$$\alpha = 2\frac{1 + 2\lambda/b}{1 + 4\lambda/b}, \tag{10}$$

approaching $\alpha = 1$ for $\lambda/b \to \infty$ [15]. For cylinders, α decreases due to the effect of the hydrodynamic slip reducing the tangential component of the hydrodynamic traction on the surface of the cylinder [15].

A. Analytical evaluation of β

The coefficient β in Eq. (9) represents the contribution to the macroscopic suspension stress from pairwise interactions. For $\lambda = 0$, Doyeux *et al.* [30] have evaluated β analytically, obtating $\beta = 3.60$. Here, we extend their method to find β as a function of λ/b.

Calculating β requires finding the short-range hydrodynamic interaction between two freely suspended cylinders centered at positions $\boldsymbol{x}_0$ and $-\boldsymbol{x}_0$, and then averaging over all possible values of $\boldsymbol{x}_0$. To find the flow disturbance due to two freely suspended cylinders, it is convenient to work in complex variables with $z = x + iy$ and $\zeta(z) = u_x + iu_y$. Here, x and y correspond to the Cartesian coordinates in a fixed frame of reference, and $\boldsymbol{u} = u_x\hat{\boldsymbol{e}}_x + u_y\hat{\boldsymbol{e}}_y$. The flow disturbance generated by a single force-free cylinder position at z_0 can be expressed in a multipole expansion (cf. [43]) as

$$\zeta_1(z') = \sum_{q=1}^{\infty} \frac{A_q}{z'^q} + \frac{q\bar{A}_q z'}{\bar{z}'^{q+1}} + \frac{B}{\bar{z}'^q}, \quad z' = z + z_0. \tag{11}$$

This expansion converges for all $|z| > b$. By symmetry, the flow field produced by the second cylinder is $\zeta_2(x) = -\zeta_1(-z)$. In complex variables, the external shear field is $\zeta_\infty = i\dot{\gamma}(\bar{z} - z)/2$. The total flow field is thus

$$\zeta(z) = \zeta_1(z') - \zeta_1(-z') + \zeta_\infty. \tag{12}$$

We approximate the hydrodynamic effect of the cylinder located at z_0 on the other cylinder by assuming that the boundary conditions only have to be satisfied for the cylinder located at z_0 [30]. For the particles to be torque-free we must have $\mathrm{Im}(B_1) = 0$ [30]. At the boundary of each particle, we assume the Navier slip boundary condition, Eq. (2). This condition translates to

$$\zeta(z_0 + be^{i\sigma}) = \zeta_0 + i\Omega be^{i\sigma} + \zeta^{\mathrm{sl}},$$

where $\sigma \in [0, 2\pi]$ is a parametrization of the boundary of the cylinder, ζ_0 is the translational velocity of the cylinder located at z_0, Ω is the angular velocity of the cylinder, and $\zeta^{\mathrm{sl}} = u_x^{\mathrm{sl}} + iu_y^{\mathrm{sl}}$ is the representation in complex variables of the slip velocity $\boldsymbol{u}^{\mathrm{sl}} = u_x^{\mathrm{sl}}\hat{\boldsymbol{e}}_x + u_y^{\mathrm{sl}}\hat{\boldsymbol{e}}_y$.

We calculate the flow field ζ using the mathematics software MAPLESOFT as follows. First, Eq. (12) is evaluated at $z_0 = r_0e^{i\theta}$. This leads to a set of algebraic equations for the unknown coefficients A_q and B_q. Next, the real and imaginary parts of A_q and B_q and the angular velocity Ω are found by assuming that each of these coefficients has an analytical expansion in powers of $2b/r_0$. Truncating this expansion to $q_{\max}$ terms, allows us to estimate the coefficients $\{A_1, \ldots, A_{q_{\max}}, B_1, \ldots, B_{q_{\max}}, \Omega\}$ to the desired accuracy. The coefficients are decomposed into a set of $4q_{\max}$ linear equations by setting each real and imaginary part of the coefficient of spectral order $e^{i\pm q\sigma}$ to zero for $q = 1, \ldots, q_{\max}$. An additional linear equation for Ω comes from the extra condition $\mathrm{Im}(B_1) = 0$. The linear system of equations is solved by Gaussian elimination.

The coefficient $\mathrm{Im}A_1$ is particularly important in determining the effective viscosity (cf. [30,31,44]). To find β, we use the expression developed by Doyeux *et al.* [30], which predicts

$$\beta = \alpha - \int_b^{\infty} \int_0^{2\pi} \mathrm{Im}A_1' \,\mathrm{d}\theta \,\mathrm{d}r_0. \tag{13}$$

Here $\mathrm{Im}(A_1')$ is the series expansion of $\mathrm{Im}(A_1)$, excluding all terms up to $O[(b/r)^2]$. The derivation of Eq. (13) is based on a mean-field approximation [3] assuming an isotropic pair-particle distribution function. The only (but important) difference with respect to the formulation given in Doyeux *et al.* is that $\mathrm{Im}(A_1')$ in the current work depends on λ.

Figure 2 shows the analytical value of β as a function of λ. The convergence of β with $q_{\max}$ (given in the inset) is slow due to the nonanalytical behavior of A_1 when the two cylinders touch each other ($r_0 = 2b$). As λ/b increases, the convergence gets even slower since the expansion in r/b becomes stiff as $\lambda/b \to \infty$. For our analytical predictions, we use $q_{\max} = 32$, the highest computed value of $q_{\max}$. For the selected values of λ given in the inset, we find that the difference in β between $q_{\max} = 32$ and $32 > q_{\max} \geqslant 18$ is smaller than 1%.

Numerical simulations of pairwise interaction of spheres [19] suggest that β decreases monotonically by about an order of magnitude for increasing λ. For the two-dimensional cylinders, our analytical calculations of β show that while there is a decrease in β for finite λ/b, the decrease in

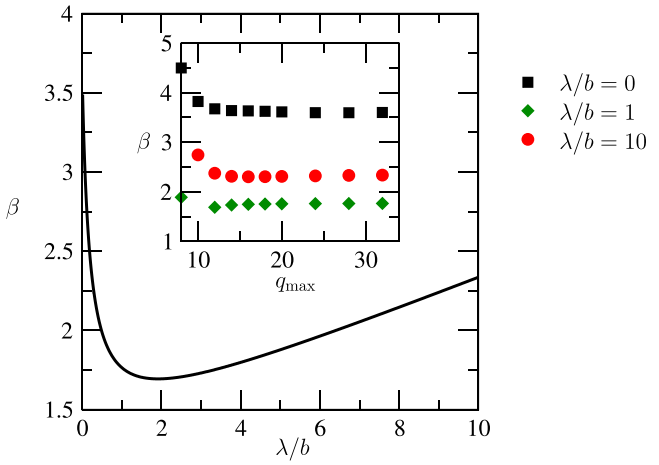

FIG. 2. Analytical prediction for β versus λ for $a/b = 1$. The prediction is based on a truncated expansion of Im(A) in powers of b/r up to order $k_{\max} = 32$. Inset: β versus $q_{\max}$ for $\lambda/b = 0$, 1, and 10.

β with λ is not monotonic. Instead $\beta(\lambda/b)$ has a minimum value $\beta = 1.69$ for $\lambda/b = 1.91$, which corresponds to roughly a 50% reduction compared to the no-slip value of β. For larger slip lengths, the general increase in β is much slower than for slip lengths smaller than the one corresponding to the minimum, so the value of β for comparatively large slip lengths (e.g., $\lambda/b = 10$) is smaller than for $\lambda = 0$.

B. Comparison between numerical and analytical estimates of $\langle\eta^{\text{eff}}\rangle$ for cylinders

Figure 3 compares the analytical prediction for $\langle\eta^{\text{eff}}\rangle$, obtained assuming an isotropic pair-particle distribution (for $q_{\max} = 32$) and retaining only the α and β terms in Eq. (9), to results computed for $\lambda/b = 0$, 1, and $\lambda/b = 10$ via the numerical procedure outlined in Sec. III. In the

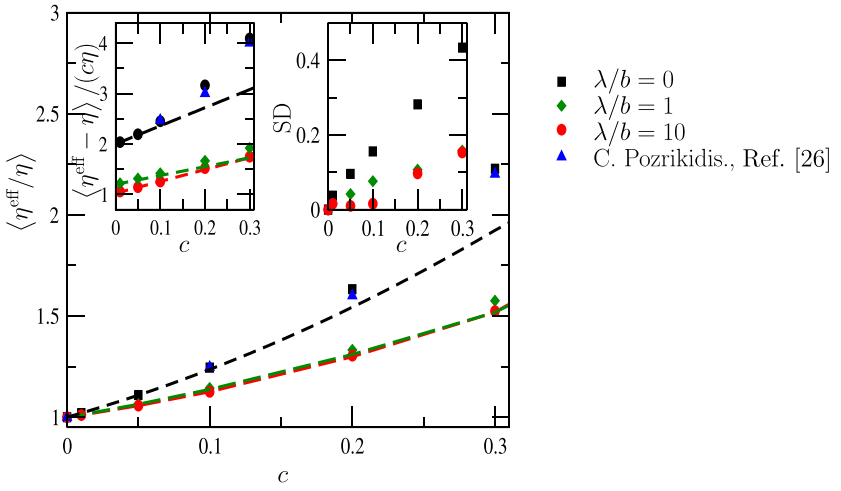

FIG. 3. Effective viscosity versus solid fraction for $a/b = 1$. Symbols represent numerical simulations; dashed lines are the analytical solution given in Eq. (9) for $\lambda/b = 0$ (black) ($\langle\eta^{\text{eff}}\rangle/\eta = 1 + 2c + 3.6c^2$), $\lambda/b = 1$ (green) ($\langle\eta^{\text{eff}}\rangle/\eta = 1 + 1.2c + 1.8c^2$), and $\lambda/b = 10$ (red) ($\langle\eta^{\text{eff}}\rangle/\eta = 1 + 1.0c + 2.3c^2$). Insets: (left) reduced viscosity versus solid fraction; (right) standard deviation (SD) of η^{eff}/η versus solid fraction.

limit $c \ll 1$ we find good agreement between the analytical and the numerical values. The numerical values confirm that the second-order coefficient β [quantified by the slope of the reduced viscosity $\langle \eta^{\text{eff}} - \eta \rangle / (c\eta)$ in the left-hand side inset of Fig. 3] is smaller for $\lambda/b = 1$ than for $\lambda/b = 10$, as predicted by the analytical solution shown in Fig. 2.

For larger values of c, our simulation results for $\lambda = 0$ compare well with the predictions of the numerical model of Ref. [26]. For larger values of c, the particle interaction is no longer pairwise, resulting in a significant deviation of $\langle \eta^{\text{eff}} \rangle$ from the analytical prediction.

In our simulations, we have also evaluated the standard deviation of η^{eff} (shown in the right-hand side inset in Fig. 3). In general, the standard deviation of η^{eff} increases as c increases due to stronger particle-particle interaction. As λ/b increases, the range of c for which the numerical value of $\langle \eta^{\text{eff}} \rangle$ is well approximated by Eq. (9) increases (as seen in the left-hand side inset) and the dependence of the standard deviation of η^{eff} with c decreases. This effect is due to slip reducing particle-particle interaction, as seen by the reduction of β with λ. As $c \to 0$, the reduced visocity $\langle \eta^{\text{eff}} - \eta) \rangle (c\eta) \to \alpha$.

Overall, these findings suggest that hydrodynamic slip reduces the effect of cylinder-cylinder interactions at higher solid fractions. In terms of the trend with respect to variations in λ, this behavior agrees qualitatively with our recent molecular dynamics simulations of suspensions of disklike molecules [7] and with the analytical theory for the effect of Navier slip on two settling spheres [45]. Also, in these studies, it was found that hydrodynamic slip reduces the effect of particle-particle interactions.

Physically, the effect of hydrodynamic slip is to reduce the tangential traction distribution over the surface of the cylinders [15]. Our analytical and computational results suggest that effect reduces both α and β in Eq. (9). Our results show that the effect of particle-particle interaction is also reduced, so that, in general, η^{eff} is significantly smaller for slip cylinders compared to no-slip cylinders and can be well approximated by Eq. (9) for a larger range of c for slip cylinders than for no-slip cylinders.

V. SIMULATIONS OF SLENDER PARTICLES AT SEMIDILUTE CONCENTRATIONS

A. Statistical convergence and validation against the dilute limit

Slender particles with $a/b \neq 1$ will reach in time a preferred orientation. Therefore, it is important to investigate how the first- and second-order orientational statistics of the particles depend on time. We show convergence of simulations with $a/b = 10$ by comparing (i) different initial conditions and (ii) different numbers of particles in the periodic domain. The time series of the instantaneous reduced viscosity and instantaneous particle orientation angle (averaged over all the particles instantaneously present in the computational domain) for three simulations at $c = 0.05$ are shown in Fig. 4. The simulations are carried out with different initial particle configurations of $N_p = 16$ particles. After a time $t\dot{\gamma} \approx 30$, the time-dependent reduced viscosity and orientation angle attain comparable mean and variance, independent of the initial condition. For $c = 0.05$ the time average values $\bar{\phi}$ (Fig. 5) and $\langle \eta^{\text{eff}} - \eta \rangle / c\eta$ (Fig. 6), and their corresponding standard deviations (SDs), do not change significantly if we change the initial condition (gray squares), or the particle number from $N_p = 16$ to $N_p = 36$ (brown diamond). This suggests that our simulations are run for a sufficient time to lose memory of the initial condition and with a sufficiently high number of particles. In Figs. 5 and 6, we also compare our simulations at finite solid fractions to dilute-limit simulations obtained by simulating a single particle [15]. A good agreement of the simulation data with the dilute-limit prediction is observed for small c.

B. Effect of slip

1. Comparing slip and no-slip particles

We begin by comparing simulations for $\lambda = 0$ and $\lambda/b = 10$, for fixed $a/b = 10$ and $c = 0.05$. A snapshot of the two cases is given in Fig. 7, and corresponding movies are given in the Supplemental

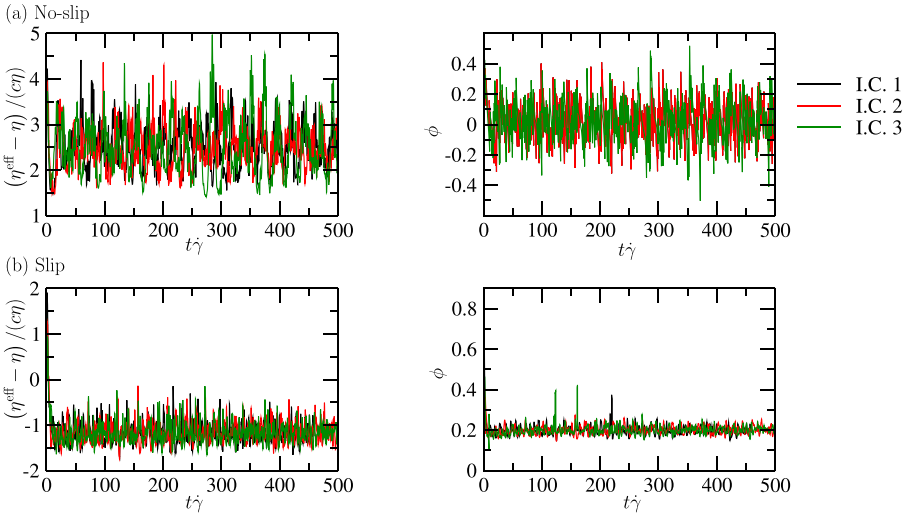

FIG. 4. Time evolution of the instantaneous reduced viscosity (left) and instantaneous particle orientation angle (right) for three different initial conditions (I.C. 1, I.C. 2, I.C. 3), and fixed $a/b = 10$, $c = 0.05$, and $N_p = 16$. The top panels are for no-slip particles, and the bottom panels are for slip particles.

Material [46]. In the slip case, the particles remain almost aligned in the flow direction. Unlike in the dilute case, however, the orientation angle is not constant: particle-particle interactions make each particle fluctuate about its average orientation. If such fluctuations were large enough, a full rotational orbit (tumbling) of the particles could occur. Instead, we found that even when the slip particles come in close contact with one another, the particle-particle interaction is not large enough to "break" the average alignment of the particles (as can be seen from the movie in Supplemental Material 2). Slip particles in close contact instead slide past each other and eventually separate, as

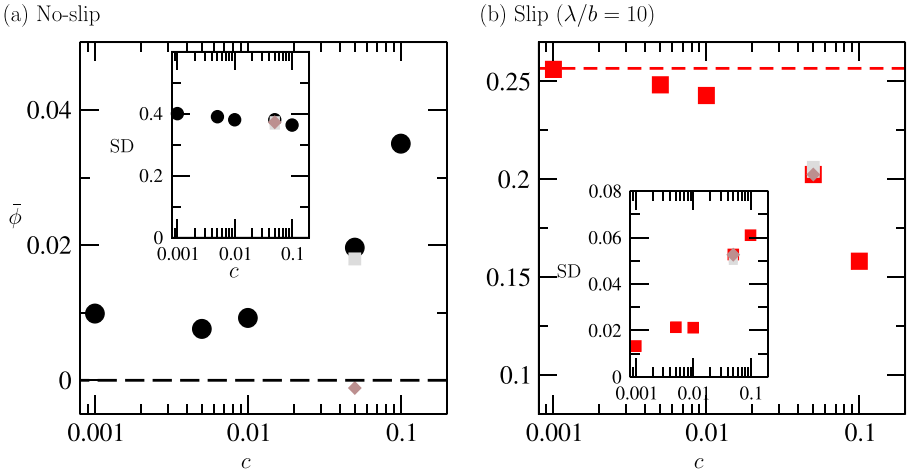

FIG. 5. Dependence of the average particle orientation on solid fraction for $a/b = 10$ and $N_p = 16$, comparing (a) no slip and (b) slip. Insets: standard deviation (SD) versus solid fraction. For $c = 0.05$, the (gray) squares correspond to data for different initial conditions and the (brown) diamonds for a suspension of 36 particles rather than 16. Dashed lines correspond to the values for an isolated particle in free space, i.e., the dilute-limit prediction [15].

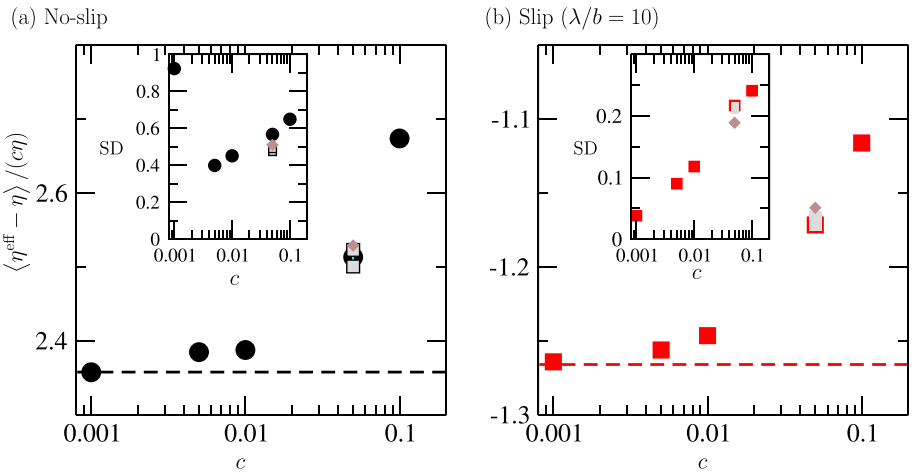

FIG. 6. Dependence of the reduced viscosity on solid fraction for $a/b = 10$, corresponding to Fig. 5, comparing (a) no slip and (b) slip. Insets: standard deviation (SD) versus solid fraction. The meaning of the symbols is as in Fig. 5.

demonstrated in Fig. 8. In the case of no-slip particles (i.e., Supplemental Material 1), full tumbling cycles occur (the particles align in the flow direction only in a time-average sense but do rotate instantaneously). An example of two particles undergoing full tumbling is given in Fig. 9.

Figure 5 shows $\bar{\phi}$ versus c for $\lambda = 0$ and $\lambda/b = 10$ (for fixed $a/b = 10$). For the no-slip case, the standard deviation of ϕ decreases slowly with c (left insert), suggesting that more particles become aligned with the flow direction as c increases due to neighboring particles limiting the rotation of each particle. This result is in agreement with simulations of no-slip two-dimensional particles with elliptical cross section [25,26] and disks [24] at semidilute concentrations. For $\lambda/b = 10$, $\bar{\phi}$ decreases with c, while the standard deviation of ϕ increases with c. As the solid fraction changes from $c = 0.001$ to $c = 0.01$, the average $\bar{\phi}$ decreases by almost a factor of 2, and the corresponding standard deviation increases by over a factor of 3. Thus, in the slip case, neighboring particles disturb the stable alignment found for $c = 0$. This result is also demonstrated in the snapshot of

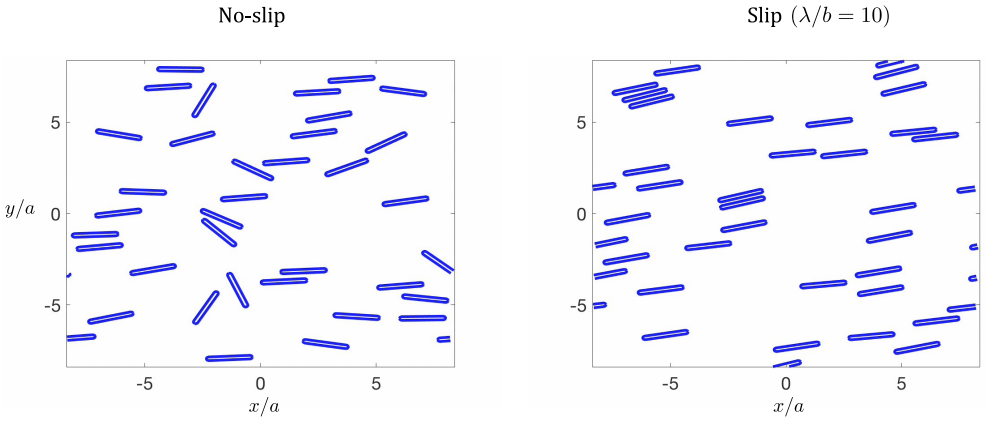

FIG. 7. Instantaneous snapshot of particle distribution for $\dot{\gamma}t = 110$ and $c = 0.05$, comparing slip and no slip. The aspect ratio and slip length are the same as in Fig. 4. Dashed lines correspond to the values for an isolated particle in free space [15].

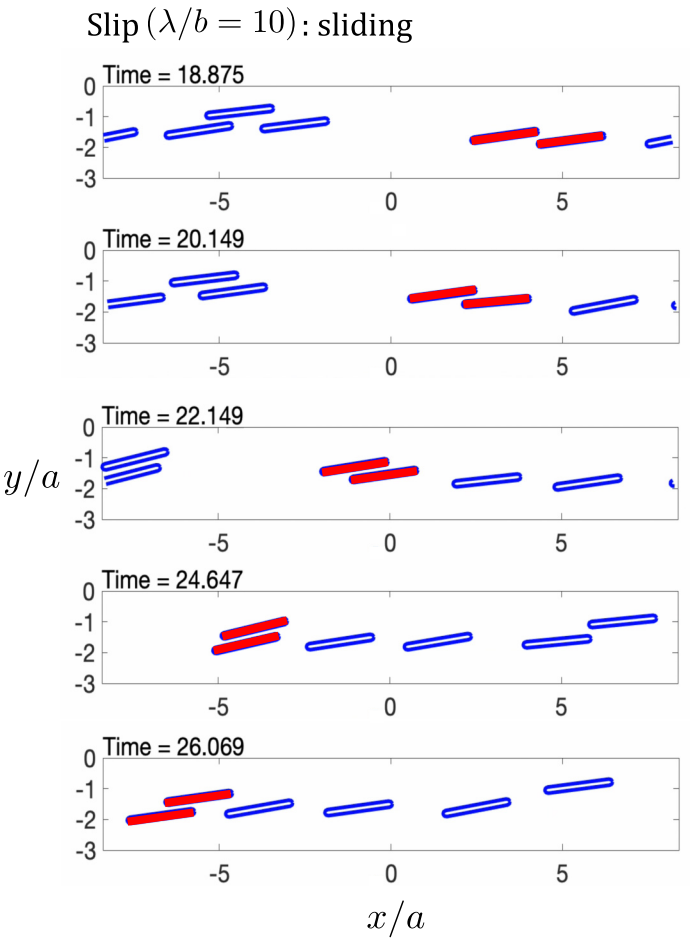

FIG. 8. Snapshot of two slip particles sliding past each other for $c = 0.05$. The particles of interest are filled (red). The particle aspect ratio and slip length are the same as in Fig. 4.

Fig. 8: the orientation angle of the particles increases as the particles slide past each other. When several particles slide past each other at the same time, sudden peaks in the time evolution of ϕ can occur, as seen for I.C. 1 and I.C. 3 in the right-hand panel of Fig. 4(b).

The reduced viscosity $\langle \eta^{\text{eff}} - \eta \rangle / (c\eta)$ (Fig. 6) is much larger for $\lambda = 0$ than for $\lambda/b = 10$ for all the values of c considered. What is most striking is that $\langle \eta^{\text{eff}} - \eta \rangle / (c\eta)$ is positive for $\lambda = 0$ and negative for $\lambda/b = 10$. In other words, for $\lambda/b = 10$, the effective shear viscosity of the suspension is smaller than the viscosity of the suspending fluid for all our computed values of c. As c increases, $\langle \eta^{\text{eff}} - \eta \rangle / (c\eta)$ increases for both $\lambda = 0$ and $\lambda/b = 10$, suggesting that particle-particle interactions increase $\langle \eta^{\text{eff}} - \eta \rangle / (c\eta)$ for both the slip and no-slip cases. For the slip case $\langle \eta^{\text{eff}} - \eta \rangle / (c\eta)$ increases from -1.26 to -1.12 as the concentration increases from $c = 0.001$ to 0.1. For the no-slip case $\langle \eta^{\text{eff}} - \eta \rangle / (c\eta)$ increases from 2.35 to 2.67 in the same range of solid concentrations. In the slip case, the reduced viscosity is negative and does not seem to reach a plateau as c increases. Therefore, there might exist a threshold value of c for which the particle effect on the effective suspension viscosity is neutral (i.e., $\langle \eta^{\text{eff}} \rangle = \eta$).

Examining the tangential force (Fig. 10), one observes that $\langle F_s \rangle$ increases slightly with c for $\lambda = 0$ and decreases slightly with c for $\lambda/b = 10$, with no significant changes to SD. For all the

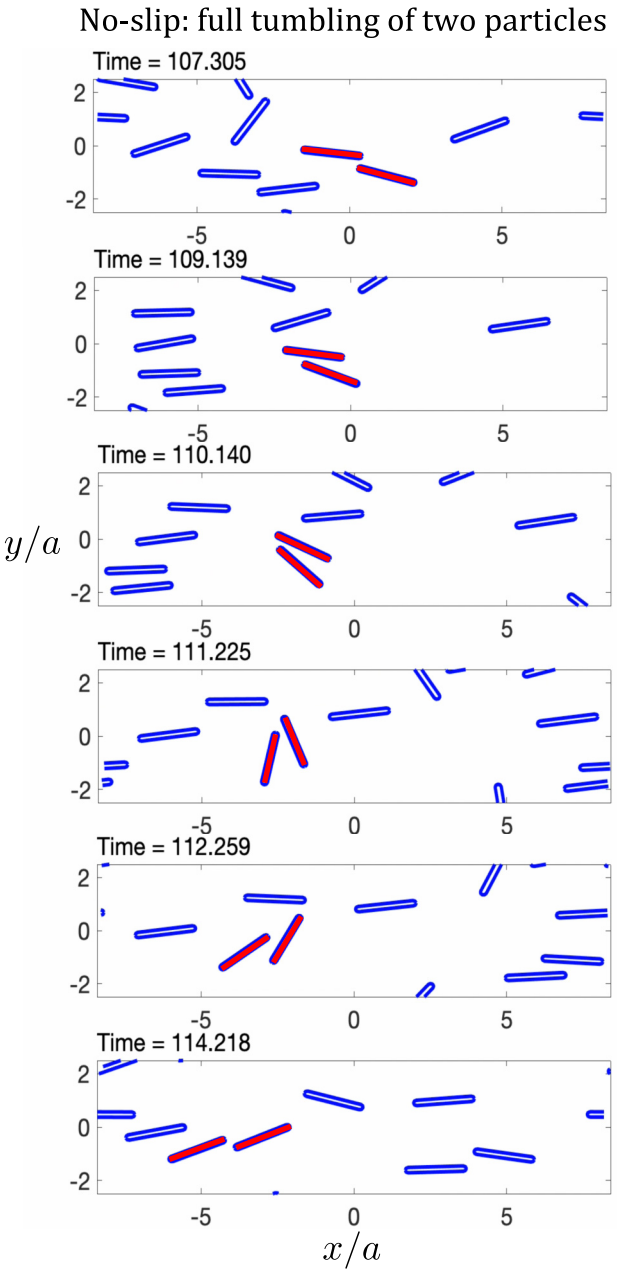

FIG. 9. Snapshot of two no-slip particles undergoing full tumbling for $c = 0.05$. The particles of interest are filled (red). The aspect ratio and slip length are the same as in Fig. 4.

solid fractions considered, $\langle F_s \rangle$ is considerably larger for $\lambda = 0$ than for $\lambda/b = 10$. This information, together with the mild dependence on c, suggests that $\langle F_s \rangle$ depends mostly on λ rather than on c in the range of solid fractions we considered.

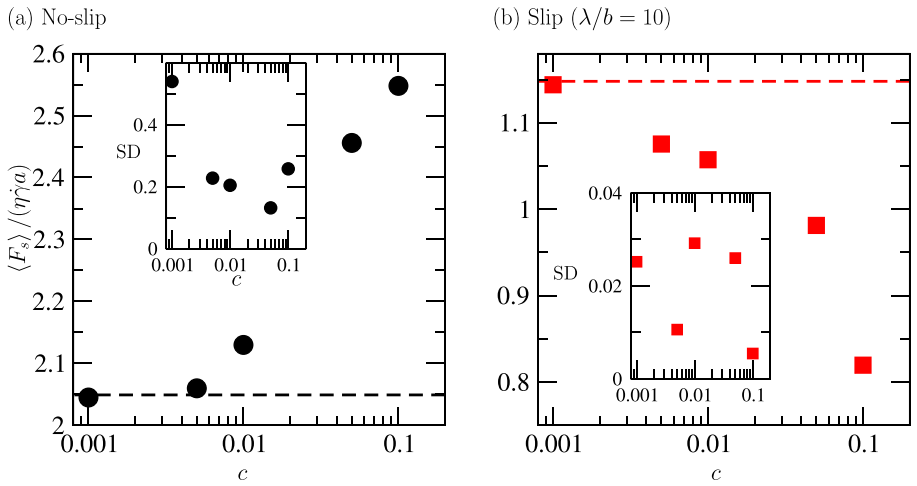

FIG. 10. Dependence of the average tangential force on solid fraction for $a/b = 10$, comparing (a) no slip and (b) slip. Insets: standard deviation (SD) versus solid fraction. Dashed lines correspond to the values for an isolated particle in free space [15].

2. *Effect of solid fraction on slip particles as a function of slip length*

Figure 11 shows $\langle \eta^{\text{eff}} - \eta \rangle / (c\eta)$, $\bar{\phi}$, and $\langle F_s \rangle$ as a function of λ/b for a single particle in free space and for 0.05. Despite the difference in solid fraction between the two cases, there is not a significant difference in $\langle \eta^{\text{eff}} - \eta \rangle / (c\eta)$ and $\bar{\phi}$. Similarly, in simulations of no-slip disklike particles with aspect ratios in the range for $a/b = 0.14-0.33$, Meng and Higdon [24] observed a significant difference in $\langle \eta^{\text{eff}} \rangle$ comparing results for finite solid fractions to the dilute limit only for solid fractions greater than $c \approx 0.25$. On the whole, $\langle \eta^{\text{eff}} - \eta \rangle / (c\eta)$, $\bar{\phi}$, and $\langle F_s \rangle$ Depend primarily on λ/a in the range $c > 0$ and $c = 0.05$. The smallest difference in all our measured mean quantities and their corresponding standard deviations occurs for $\lambda \approx \lambda_c$. Here, $\lambda_c \simeq b$ corresponds to the minimum value of λ for which an isolated particle aligns indefinitely in the flow.

Our simulations indicate that different dependencies of $\langle \eta^{\text{eff}} - \eta \rangle / (c\eta)$, $\bar{\phi}$, and $\langle F_s \rangle$ on c hold depending on whether λ is larger or smaller than λ_c. If $\lambda < \lambda_c$, the particles become more aligned with the flow (in a time-average sense) as c increases; else, if $\lambda > \lambda_c$, the particles become less aligned (middle panel), due to particle-particle interactions. For large λ, $\langle \eta^{\text{eff}} - \eta \rangle / (c\eta)$ (left panel)

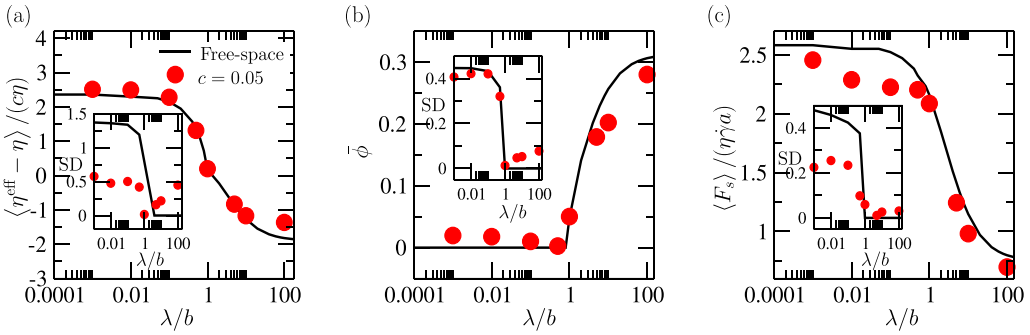

FIG. 11. Dependence of reduced viscosity (left panel), average particle orientation (middle panel), and average tangential force (right panel) on slip length for $c = 0.05$ (symbols) and for an isolated particle in free space (line). The aspect ratio is $a/b = 10$. Insets: standard deviation (SD) versus solid fraction.

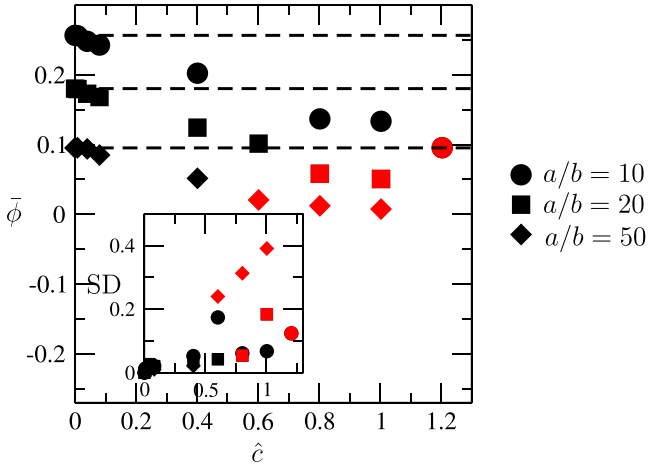

FIG. 12. Dependence of average particle orientation on $\hat{c} = N\pi a^2/A$ for selected aspect ratios and $\lambda/b = 10$. Black symbols: no full tumbling observed; red symbols: full tumbling of one or more particles observed. Insets: standard deviation (SD) versus solid fraction. Dashed lines correspond to the values for an isolated particle in free space [15].

tends to a constant whose value depends on c. When $\lambda < \lambda_c$, $\langle \eta^{\text{eff}} - \eta \rangle/(c\eta)$ is larger for $c = 0.05$ than for the isolated particle. Increasing λ for $\lambda < \lambda_c$ and fixed c instead decreases $\langle \eta^{\text{eff}} - \eta \rangle/(c\eta)$. As in the case of no-slip particles, slip particles become more aligned with the flow in a time-average sense as the concentration increases due to neighboring particles limiting the rotation of each particle, Fig. 11(b). Regarding $\langle F_s \rangle$ (right panel), the dependence of this quantity on λ is qualitatively similar to that of $\langle \eta^{\text{eff}} - \eta \rangle/(c\eta)$, except that when $\lambda < \lambda_c$ the change between $c = 0.05$ and an isolated particle is larger when considering the tangential force as opposed to the reduced viscosity.

3. Effect of aspect ratio on slip particles

Figure 12 shows $\bar{\phi}$ as a function of $\hat{c} = N\pi a^2/A$ for $a/b = 10$, 20, and 50 and fixed $\lambda/b = 10$. The parameter $\hat{c} = N\pi a^2/A$ is chosen as a measure of crowdedness, as this quantity represents the solid concentration corresponding to a cylinder of radius equal to the long semiaxis of the particle. We expect strong interactions for $\hat{c}$ sufficiently close to one, independently of the thickness.

Figure 12 shows that as $\hat{c} \to 0$, the simulated value of the orientation angle $\bar{\phi}$ converges to the dilute-limit predictions [15]. In this limit, slip particles with $\lambda > \lambda_c$ attain a fixed orientation angle ϕ_c that decreases as a/b increases [6,8]. Figure 12 shows that as $\hat{c}$ increases, $\bar{\phi}$ decreases and the standard deviation of ϕ increases. Eventually, above a threshold solid fraction, the fluctuations induced by particle-particle interaction cause some of the particles to undergo full tumbling cycles.

In Fig. 12, simulations where at least one particle tumbled during the simulation are colored in red. When tumbling occurs, $\bar{\phi}$ is comparatively small and the standard deviation of ϕ is relatively large, confirming the predictions of Ref. [8]. For an isolated particle, $\bar{\phi}$ decreases for increasing aspect ratios [8] and the range of values of ϕ for which the particle remains in a stable "hydrodynamic well" decreases [8]. The particle orientation is, therefore, more sensitive to disturbances as the aspect ratio is increased. Consequently, tumbling is expected to occur at a smaller value of $\hat{c}$ the higher the aspect ratio of the particles. This behavior is confirmed by our simulations: for $a/b = 50$, the particles tumble at a lower value of $\hat{c}$ than for $a/b = 20$ or $a/b = 10$.

In our simulations, we find that $\langle \eta^{\text{eff}} - \eta \rangle/(c\eta)$ always increases with $\hat{c}$ (Fig. 13). The rate of increase in $\langle \eta^{\text{eff}} - \eta \rangle/(c\eta)$ with $\hat{c}$ is larger if tumbling occurs. This can be seen in the simulations with $a/b = 50$, where the largest increase in $\langle \eta^{\text{eff}} - \eta \rangle/(c\eta)$ is observed for values of $\hat{c}$ above approximately 0.4. If no tumbling occurs, the rate of increase in $\langle \eta^{\text{eff}} - \eta \rangle/(c\eta)$ with $\hat{c}$ is comparatively

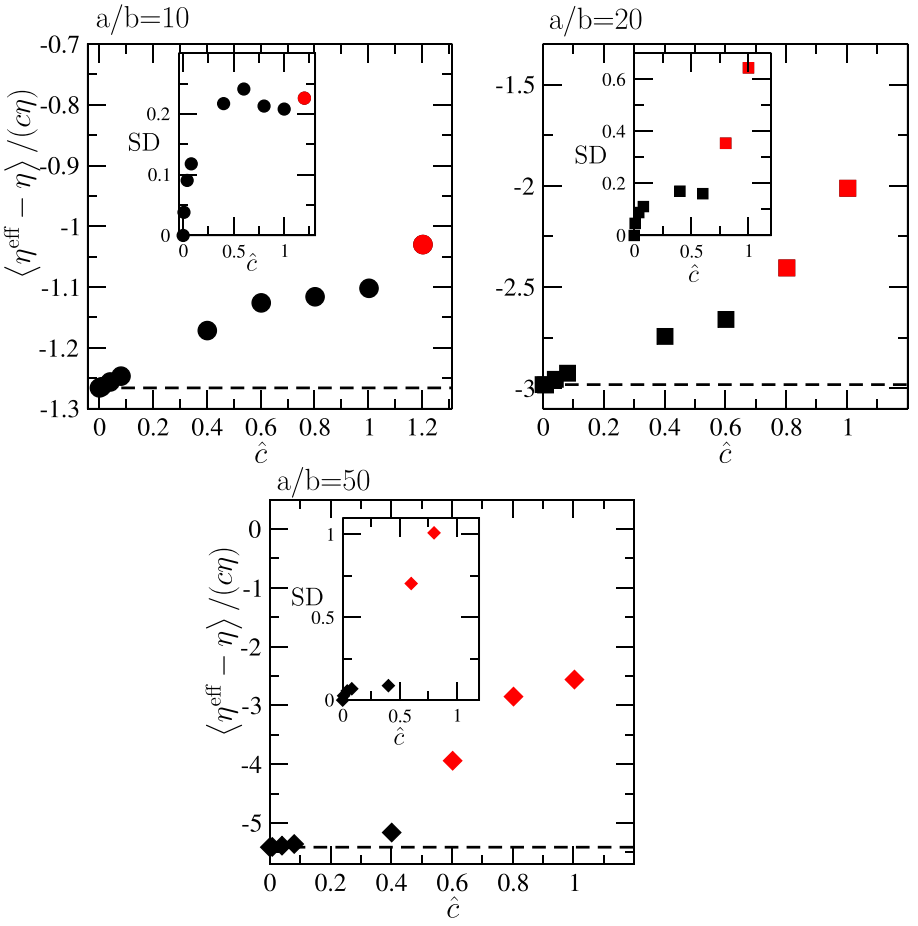

FIG. 13. Dependence of reduced viscosity on $\hat{c} = N\pi a^2/A$ for selected aspect ratios and $\lambda/b = 10$. Black symbols: no full tumbling observed; red symbols: full tumbling of one or more particles observed. Insets: standard deviation (SD) versus solid fraction.

small. In this case, $\eta^{\rm eff}$ is well approximated by the linear dependence $\eta^{\rm eff}/\eta \approx 1 + \alpha c$ expected in the dilute limit, as confirmed in Fig. 14. In a recent molecular dynamics simulation study of suspensions of disklike molecules, it was observed that the dilute approximation for $\langle \eta^{\rm eff} \rangle$ held for a larger value of $\hat{c}$ when the intermolecular solid-liquid interaction potential was such that the molecules presented slip rather than no slip [7]. Our results suggest that this phenomenon is due to the suppression of the tumbling of the particles produced by the hydrodynamic slip.

Examining $\langle F_s \rangle$, we observe a small decrease in $\langle F_s \rangle$ with $\hat{c}$, Fig. 15. When tumbling occurs, the change of $\langle F_s \rangle$ and its corresponding SD with $\hat{c}$, is not as significant as the change in $\langle \eta^{\rm eff} - \eta \rangle / (c\eta)$ with $\hat{c}$. This result suggests that, in the range of concentrations we considered, the particles experience a similar average tangential force regardless of concentration.

C. Maximum viscosity reduction

Figure 14 shows $\langle \eta^{\rm eff}/\eta \rangle$ versus c for $\lambda = 0$ and $\lambda/b = 10$, and for $a/b = 1$, 10, 20, and 50. As predicted by the theory for a dilute suspension of slip particles [15], the simulations show that $\langle \eta^{\rm eff}/\eta \rangle < 1$ for $a/b \geqslant 10$ and $\lambda/b = 10$ for all computed values of c. According to the dilute limit, indicated by the dashed lines in the plot, the larger the value of a/b, the greater the decrease

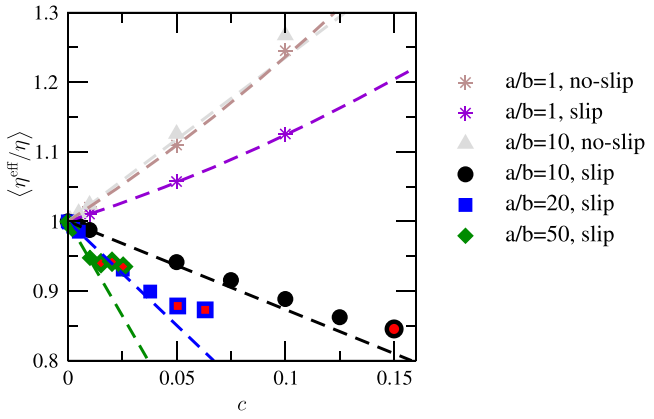

FIG. 14. Effective viscosity versus solid fraction for selected aspect ratios, comparing slip ($\lambda/b = 10$) and no-slip particles. Dashed lines correspond to (i) Eq. (9) for $a/b = 1$ and (ii) the dilute approximation ($\langle \eta^{\rm eff}/\eta \rangle = 1 + \alpha c$) for all other aspect ratios. Simulations with one or more particles completing full tumbling are indicated by symbols filled in red.

in $\langle \eta^{\rm eff}/\eta \rangle$ for a fixed c. The simulations, however, show that this trend no longer holds in the semidilute regime. For slip particles, the larger a/b, the smaller the value of c for which the particles tumble. As seen for $a/b = 50$ and $a/b = 20$, $\langle \eta^{\rm eff}/\eta \rangle$ decreases less rapidly with c when tumbling occurs, causing $\langle \eta^{\rm eff}/\eta \rangle$ to level off at larger solid fractions. Therefore, our simulations suggest that for particles of a fixed λ/b, the greatest reduction in $\langle \eta^{\rm eff}/\eta \rangle$ is achieved for finite values of a/b and c. For example, in our simulations, the largest reduction is achieved for $a/b = 10$ and $c = 0.15$.

D. Regular arrays

Our simulations show a strong correlation between the orientation of the particles and $\langle \eta^{\rm eff} \rangle$. In a recent publication [15], we have shown theoretically and numerically that, in the dilute

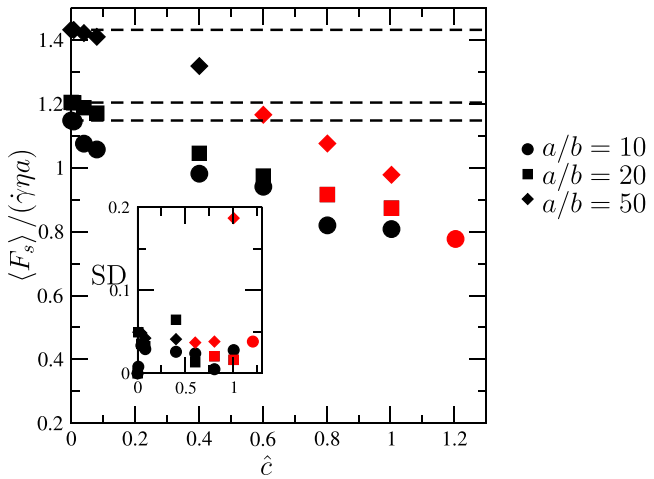

FIG. 15. Dependence of average tangential force on $\hat c = N\pi a^2/A$ for selected aspect ratios and $\lambda/b = 10$. Black symbols: no full tumbling observed; red symbols: full tumbling of one or more particles observed. Insets: standard deviation (SD) versus solid fraction.

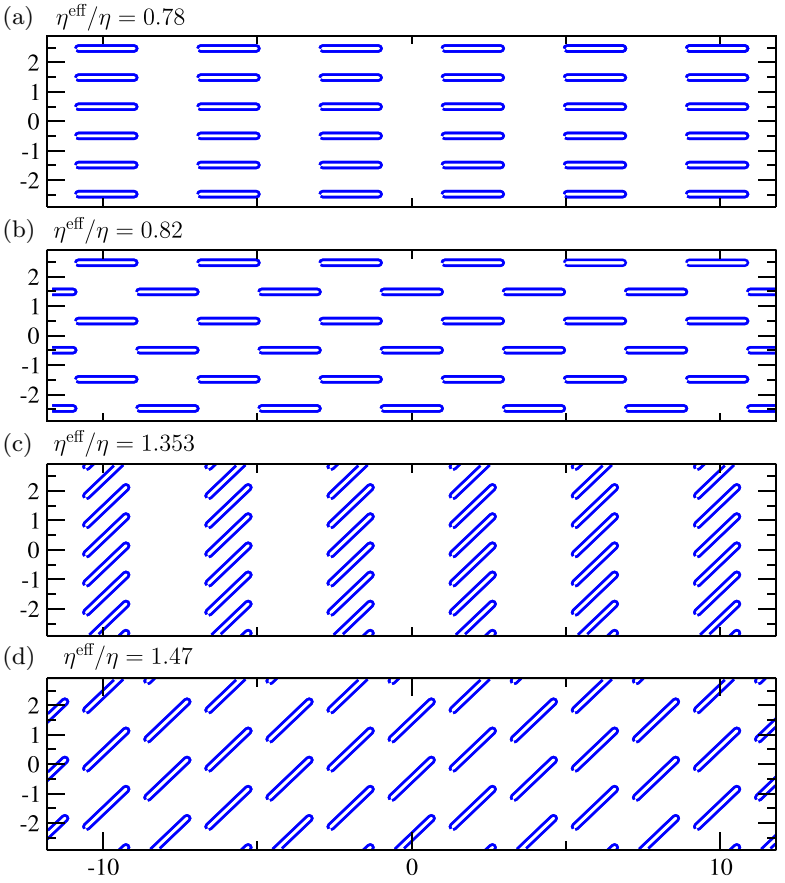

FIG. 16. Effective viscosity for regular periodic arrays of aligned slip particles for (a) $\phi = 0$, rectangular array; (b) $\phi = 0$, staggered array; (c) $\phi = \pi/4$, rectangular array; and (d) $\phi = \pi/4$, staggered array. The solid fraction is $c = 0.1$. The particle aspect ratio and slip length are the same as in Fig. 4.

concentration limit, $\langle \eta^{\text{eff}} \rangle$ depends strongly on orientation. Specifically, the smallest $\langle \eta^{\text{eff}} \rangle$ occurs when the particle's major axis is oriented along the flow ($\phi = 0$). The largest value of $\langle \eta^{\text{eff}} \rangle$ occurs when the particle's major axis is oriented in the extensional axis of the shear flow field ($\phi = \pi/4$), independently of λ. These results, along with the simulation results of the current paper, demonstrate that the orientation and position of the suspended particles strongly affect $\langle \eta^{\text{eff}} \rangle$ for any value of c and that the dilute theory gives a good indication of the orientations for which $\langle \eta^{\text{eff}} \rangle$ is minimal. To illustrate this point, in Fig. 16, we compute η^{eff} for regular arrays in which (i) the particles are oriented at $\phi = 0$ in a rectangular (a) and staggered (b) array and (ii) the particles are oriented at $\phi = \pi/4$ in a rectangular (c) and staggered (d) array. These simulations give $\eta^{\text{eff}}/\eta < 1$ for $\phi = 0$ and $\eta^{\text{eff}}/\eta > 1$ for $\phi = \pi/4$, as in the dilute case. The rectangular array gives a smaller η^{eff} than a staggered array. Therefore, both the positional and the orientational order of the suspension will affect the value of η^{eff}.

VI. DISCUSSION AND CONCLUSION

Through boundary integral simulations and, where possible, mathematical analysis, we have investigated the effect of Navier slip on the flow and rheology of an infinite Péclet number, semidilute suspension of two-dimensional particles for aspect ratios $a/b = 1, 10, 20$, and 50. In

particular, we have analyzed as a function of the solid fraction c the effect of the Navier slip length λ on the suspensions' effective viscosity $\langle \eta^{\mathrm{eff}} \rangle$, average particle orientation angle $\bar{\phi}$, and average tangential force $\langle F_s \rangle$ acting on each particle.

For the case $a/b = 1$, which corresponds to a cylindrical cross section, we showed analytically and through boundary integral computations that hydrodynamic slip reduces the $O(c)$ intrinsic viscosity coefficient α at dilute concentration and the $O(c^2)$ viscosity coefficient β at semidilute concentration. This effect is due to hydrodynamic slip reducing the tangential stress over the surface of the cylinder and the hydrodynamic stress generated from pairwise interactions.

For larger aspect ratios, the orientational microstructure of the particles becomes important. For $a/b \gg 1$, $c \ll 1$, and $\lambda > \lambda_c$, where $\lambda_c \sim b$ is a critical slip length [15], hydrodynamic slip suppresses the tumbling of the particles, causing each particle to align at a small constant angle with respect to the flow direction (for $a/b \gg 1$ the angle can be quantified as $\phi_c \approx |k_e|$, where k_e is a function of both a/b and λ/b [15]). Therefore, for $c \ll 1$ and $\lambda > \lambda_c$, the time-averaged orientation angle $\bar{\phi} = \phi_c$ with zero standard deviation. The simulations show that as c increases, the effect of particle-particle interaction is to cause the particles to fluctuate about their average orientation. As c increases, the standard deviation of ϕ increases, while the mean value of ϕ decreases. Above a threshold solid fraction, particle-induced fluctuations eventually become larger than the range of value of ϕ for which the orientation is stable [15] and the particles can therefore tumble. We found that this threshold solid fraction decreases as a/b increases. This dependence on a/b is due to the fact that the range of values of ϕ for which an isolated particle is "attracted" to a stable orientation ϕ_c decreases with a/b [8]. This result contrasts with simulations of no-slip particles, where the average orientation angle becomes smaller as c increases (due to particle-particle interaction increasing the average time for a particle to tumble [23–27]).

The behavior of $\langle \eta^{\mathrm{eff}} \rangle$ versus c correlates with orientational microstructure. For $c \ll 1$, $\langle \eta^{\mathrm{eff}}/\eta \rangle$ decreases with c for $\lambda > \lambda_c$, resulting in $\langle \eta^{\mathrm{eff}}/\eta \rangle < 1$. This behavior results from the stable orientation of the particle almost in the flow direction and from the reduced viscous friction at this orientation. We developed a dilute-limit theory for $\langle \eta^{\mathrm{eff}}/\eta \rangle$ and $\lambda > \lambda_c$. This theory provides a good estimate for $\langle \eta^{\mathrm{eff}}/\eta \rangle$ also in the semidilute range, as long as the particles do not tumble. When the particles begin to tumble, the reduced viscosity $\langle \eta^{\mathrm{eff}} - \eta \rangle/(c\eta)$ is larger than the value predicted by the dilute theory.

For slip particles, the emergence of tumbling directly affects the minimum value of $\langle \eta^{\mathrm{eff}}/\eta \rangle$ achievable. For a fixed $\lambda > \lambda_c$, $\langle \eta^{\mathrm{eff}}/\eta \rangle$ decreases as a/b increases for $c \ll 1$. However, at sufficiently high solid fractions, this relationship no longer holds: a particle of a higher aspect ratio will begin to tumble at a smaller solid fraction than a particle of a smaller aspect ratio. Therefore, an optimal aspect ratio and solid fraction exist for which the reduction in $\langle \eta^{\mathrm{eff}}/\eta \rangle$ is greatest. For example, in our simulations, we find the largest reduction in $\langle \eta^{\mathrm{eff}}/\eta \rangle$ occurred for $\lambda/b = 10$, $a/b = 10$, and $c = 0.15$ (cf. Fig. 14). Because particle-particle interactions depend on the minimal separation distance, we suspect that significant reductions in viscosity could be achieved if the particles could be kept well separated, for instance, by exploiting electrostatic repulsion or by adding molecular dispersants that do not alter the hydrodynamics behavior discussed here.

The most significant effect on $\langle \eta^{\mathrm{eff}} \rangle$ is apparent when comparing slip and no-slip particles. Surface slip reduces $\langle \eta^{\mathrm{eff}}/\eta \rangle$ below the value obtained for $\lambda = 0$ for any value of c and a/b we have simulated. For particles with sufficiently large a/b and $\lambda/\lambda_c > 1$, the particles reduce the viscosity of the two-phase mixture below the viscosity of the suspending fluid. This result can help explain some of the differences observed between suspensions of platelike nanomaterials at small solid fractions and classical theories on the viscosity of suspensions of no-slip particles. For example, experimental results for η^{eff} for graphene-oxide nanoparticles in a steady shear flow in the limit of small solid fractions show a nonmonotonic increase in η^{eff} with solid fraction at high shear rates [2]. These experiments suggest a threshold (small) solid fraction for which η^{eff} is locally minimized. Our theory suggests that this threshold solid fraction could result from the breakdown of the stable alignment of the particles when the solid fraction increases. A similar disturbance effect of particle-particle interaction on orientation was also recently discussed for rigid no-slip rings, which

can display a stable alignment [47]. In contrast to slip platelets, no-slip rings do not seem to display a negative intrinsic viscosity [48].

Finally, we explored the effect of solid fraction, aspect ratio, and hydrodynamic slip on the average tangential force $\langle F_s \rangle$ acting on each particle. We found that the dependence of $\langle F_s \rangle$ and the standard deviation of F_s on c was not as strong as for $\langle \eta^{\text{eff}}/\eta \rangle$, suggesting the dilute-limit value of $\langle F_s \rangle$ could be used to estimate, for example, the sliding force acting on each particle in a sheared suspension at relatively high values of c. Such force is required, for example, to predict the conditions for multilayer nanomaterials to separate into fewer-layer sheets, as considered by Gravelle *et al.* [32] for an isolated graphene multilayer.

Our results, based on two-dimensional simulations, are expected to agree qualitatively with the rheological behavior of three-dimensional platelike particles with hydrodynamic slip. The single-particle theory for two-dimensional platelike particles has already been shown to give good agreement to three-dimensional simulations in predicting the particle's orientation, dynamics, and effective viscosity for different slip lengths, aspect ratios, and Péclet numbers [6,7,15]. We expect good agreement in terms of trends between two dimensions and three dimensions for $\langle \eta^{\text{eff}} \rangle$ and $\langle F_s \rangle$ in suspensions as well.

One important implication of our results is the effect of particle orientation on the viscosity reduction. Our results suggest that the effect of slip on reducing the effective viscosity is most apparent when the particles are aligned indefinitely in the flow direction. In a recent publication, it has been found that in a Taylor-Couette flow, elongated particles can get trapped in the Taylor vortex cores and align strongly with the local cylinder tangent [49]. Our result suggests that the resistance of the flow of the fluid could also be minimized in such an event due to the alignment of the particles. Considering in the simulation elements of nonideality that are typically present in realistic nanoparticle systems, such as the addition of dispersants or the modification of the particle surface charge to increase the separation of the particles, could also be explored to minimize the effect of particle-particle interaction at larger solid fractions. Minimizing the effect of particle interaction would thus increase the critical solid fraction threshold for which the particles will tumble.

ACKNOWLEDGMENTS

C.K. would like to thank Alexander Farutin for his helpful discussion on the MAPLESOFT implementation of the algorithm used in Sec. IV. Funding from the Stokes Research Fellowship, Pembroke College, Cambridge, is gratefully acknowledged (C.K.). L.B. and C.K. gratefully acknowledge funding from the European Research Council (ERC) under the European Union's Horizon 2020 research and innovation program (Grant Agreement No. 715475, project FlexNanoFlow).

[1] H. Xiao and S. Liu, 2D nanomaterials as lubricant additive: A review, Mater. Des. **135**, 319 (2017).

[2] F. Del Giudice and A. Q. Shen, Shear rheology of graphene oxide dispersions, Curr Opin. Chem. Eng. **16**, 23 (2017).

[3] S. Kim and S. J. Karrila, *Microhydrodynamics: Principles and Selected Applications* (Courier Corporation, North Chelmsford, MA, 2013).

[4] X. He, H. Xiao, J. P. Kyle, E. J. Terrell, and H. Liang, Two-dimensional nanostructured Y_2O_3 particles for viscosity modification, Appl. Phys. Lett. **104**, 163107 (2014).

[5] X. He, H. Xiao, H. Choi, A. Díaz, B. Mosby, A. Clearfield, and H. Liang, α-Zirconium phosphate nanoplatelets as lubricant additives, Colloids Surf. A **452**, 32 (2014).

[6] C. Kamal, S. Gravelle, and L. Botto, Hydrodynamic slip can align thin nanoplatelets in shear flow, Nat. Commun. **11**, 2425 (2020).

[7] S. Gravelle, C. Kamal, and L. Botto, Violations of Jeffery's theory in the dynamics of nanographene in shear flow, Phys. Rev. Fluids **6**, 034303 (2021).
[8] C. Kamal, S. Gravelle, and L. Botto, Effect of hydrodynamic slip on the rotational dynamics of a thin Brownian platelet in shear flow, J. Fluid Mech. **919**, A1 (2021).
[9] C. Kamal, S. Gravelle, and L. Botto, Alignment of a flexible plate-like particle in shear flow: Effect of surface slip and edges, Phys. Rev. Fluids **6**, 084102 (2021).
[10] A. Maali, T. Cohen-Bouhacina, and H. Kellay, Measurement of the slip length of water flow on graphite surface, Appl. Phys. Lett. **92**, 053101 (2008).
[11] D. Ortiz-Young, H.-C. Chiu, S. Kim, K. Voïtchovsky, and E. Riedo, The interplay between apparent viscosity and wettability in nanoconfined water, Nat. Commun. **4**, 2482 (2013).
[12] G. Tocci, L. Joly, and A. Michaelides, Friction of water on graphene and hexagonal boron nitride from ab initio methods: Very different slippage despite very similar interface structures, Nano Lett. **14**, 6872 (2014).
[13] G. B. Jeffery, The motion of ellipsoidal particles immersed in a viscous fluid, Proc. R. Soc. London, Ser. A **102**, 161 (1922).
[14] D. G. Crowdy, Equilibrium tilt of slippery elliptical rods in creeping simple shear, J. Fluid Mech. **931**, R2 (2022).
[15] C. Kamal and L. Botto, The effect of Navier slip on the rheology of a dilute two-dimensional suspension of plate-like particles, J. Fluid Mech. **972**, A1 (2023).
[16] C. Pozrikidis, *Boundary Integral and Singularity Methods for Linearized Viscous Flow* (Cambridge University Press, Cambridge, UK, 1992).
[17] D. Malhotra and A. Barnett, Efficient convergent boundary integral methods for slender bodies, J. Comput. Phys. **503**, 112855 (2024).
[18] S. A. Allison, Low Reynolds number transport properties of axisymmetric particles employing stick and slip boundary conditions, Macromolecules **32**, 5304 (1999).
[19] H. Luo and C. Pozrikidis, Interception of two spheres with slip surfaces in linear Stokes flow, J. Fluid Mech. **581**, 129 (2007).
[20] H. Luo and C. Pozrikidis, Effect of surface slip on Stokes flow past a spherical particle in infinite fluid and near a plane wall, J. Eng. Math. **62**, 1 (2008).
[21] C. J. S. Petrie, The rheology of fibre suspensions, J. Non-Newton. Fluid Mech. **87**, 369 (1999).
[22] R. R. Sundararajakumar, D. L. Koch, and E. S. G. Shaqfeh, The extensional viscosity and effective thermal conductivity of a dispersion of aligned disks, Phys. Fluids **6**, 1955 (1994).
[23] S. Yamamoto and T. Matsuoka, Dynamic simulation of a plate-like particle dispersed system, J. Chem. Phys. **107**, 3300 (1997).
[24] Q. Meng and J. J. L. Higdon, Large scale dynamic simulation of plate-like particle suspensions. Part I: Non-Brownian simulation, J. Rheol. **52**, 1 (2008).
[25] C. Pozrikidis, Dynamic simulation of the flow of suspensions of two-dimensional particles with arbitrary shapes, Eng. Anal. Boundary Elem. **25**, 19 (2001).
[26] C. Pozrikidis, Orientation statistics and effective viscosity of suspensions of elongated particles in simple shear flow, Eur. J. Mech., B: Fluids **24**, 125 (2005).
[27] C. H. Hsueh and W. C. J. Wei, Effective viscosity of semidilute suspensions of rigid ellipsoids, J. Appl. Phys. **107**, 024905 (2010).
[28] J. Guo, Q. Zhou, and R. Chik-Kwong Wong, Effects of volume fraction and particle shape on the rheological properties of oblate spheroid suspensions, Phys. Fluids **33**, 081703 (2021).
[29] J. F. Brady, The Einstein viscosity correction in n dimensions, Int. J. Multiphase Flow **10**, 113 (1983).
[30] V. Doyeux, S. Priem, L. Jibuti, A. Farutin, M. Ismail, and P. Peyla, Effective viscosity of two-dimensional suspensions: Confinement effects, Phys. Rev. Fluids **1**, 043301 (2016).
[31] G. K. Batchelor, The stress system in a suspension of force-free particles, J. Fluid Mech. **41**, 545 (1970).
[32] S. Gravelle, C. Kamal, and L. Botto, Liquid exfoliation of multilayer graphene in sheared solvents: A molecular dynamics investigation, J. Chem. Phys. **152**, 104701 (2020).
[33] S. Chen, Q. Li, D. He, Y. Liu, L. Wang, and M. Wang, Dynamic exfoliation of graphene in various solvents: All-atom molecular simulations, Chem. Phys. Lett. **804**, 139900 (2022).

[34] K. R. Paton, J. Anderson, A. J. Pollard, and T. Sainsbury, Production of few-layer graphene by microfluidization, Mater. Res. Express **4**, 025604 (2017).
[35] P. G. Karagiannidis, S. A. Hodge, L. Lombardi, F. Tomarchio, N. Decorde, S. Milana, I. Goykhman, Y. Su, S. V. Mesite, and D. N. Johnstone, Microfluidization of graphite and formulation of graphene-based conductive inks, ACS Nano **11**, 2742 (2017).
[36] K. R. Paton, E. Varrla, C. Backes, R. J. Smith, U. Khan, A. O'Neill, C. Boland, M. Lotya, O. M. Istrate, P. King *et al.*, Scalable production of large quantities of defect-free few-layer graphene by shear exfoliation in liquids, Nat. Mater. **13**, 624 (2014).
[37] J. Stafford, N. Uzo, U. Farooq, S. Favero, S. Wang, H.-H. Chen, A. L'Hermitte, C. Petit, and O. K. Matar, Real-time monitoring and hydrodynamic scaling of shear exfoliated graphene, 2D Mater. **8**, 025029 (2021).
[38] A. W. Lees and S. F. Edwards, The computer study of transport processes under extreme conditions, J. Phys. C: Solid State Phys. **5**, 1921 (1972).
[39] C. Pozrikidis, Orbiting motion of a freely suspended spheroid near a plane wall, J. Fluid Mech. **541**, 105 (2005).
[40] C. Pozrikidis, *A Practical Guide to Boundary Element Methods with the Software Library BEMLIB* (CRC Press, Boca Raton, FL,2002).
[41] J. Eggers and M. A. Fontelos, *Singularities: Formation, Structure, and Propagation* (Cambridge University Press, Cambridge, 2015).
[42] M. Belzons, R. Blanc, J. L. Bouillot, and C. Camoin, Viscosité d'une suspension diluée et bidimensionnelle de sphères, C. R. Acad. Sci. Paris, Ser. 2 **292**, 939 (1981).
[43] A. Farutin, H. Wu, W.-F. Hu, S. Rafaï, P. Peyla, M.-C. Lai, and C. Misbah, Analytical study for swimmers in a channel, J. Fluid Mech. **881**, 365 (2019).
[44] J. Happel and H. Brenner, *Low Reynolds Number Hydrodynamics with Special Application to Particulate Media* (Prentice-Hall, Englewood Cliffs, NJ, 1965).
[45] H. J. Keh and S. H. Chen, Low-Reynolds-number hydrodynamic interactions in a suspension of spherical particles with slip surfaces, Chem. Eng. Sci. **52**, 1789 (1997).
[46] See Supplemental Material at http://link.aps.org/supplemental/10.1103/PhysRevFluids.9.074102 for videos of simulations of sheared particles with and without hydrodynamic slip in a periodic domain.
[47] N. S. Borker, A. D. Stroock, and D. L. Koch, Robust microstructure of self-aligning particles in a simple shear flow, Phys. Rev. Fluids **9**, 043301 (2024).
[48] N. S. Borker and D. L. Koch, Shear rheology of a dilute suspension of thin rings, J. Rheol. **67**, 723 (2023).
[49] M. P. A. Assen, C. S. Ng, J. B. Will, R. J. A. M. Stevens, D. Lohse, and R. Verzicco, Strong alignment of prolate ellipsoids in Taylor–Couette flow, J. Fluid Mech. **935**, A7 (2022).